Event patterns from negative pion spectra in proton-proton and nucleus-nucleus collisions at SPS

Ya-Hui Chen[1], Fu-Hu Liu[1;*], Edward K. Sarkisyan-Grinbaum[2;3;†]

[1] *Institute of Theoretical Physics & State Key Laboratory of Quantum Optics and Quantum Optics Devices, Shanxi University, Taiyuan, Shanxi 030006, China*

[2] *Experimental Physics Department, CERN, 1211 Geneva 23, Switzerland*

[3] *Department of Physics, The University of Texas at Arlington, Arlington, TX 76019, USA*

Abstract: Rapidity-dependent transverse momentum spectra of negatively charged pions measured at different rapidities in proton-proton collisions at the Super Proton Synchrotron (SPS) at various energies within its Beam Energy Scan (BES) program are investigated by using one- and two-component standard distributions where the chemical potential and spin property of particles are implemented. The rapidity spectra are described by a double-Gaussian distribution. At the stage of kinetic freeze-out, the event patterns are structured by the scatter plots in the three-dimensional subspaces of velocity, momentum and rapidity. The results of the studies of the rapidity-independent transverse mass spectra measured at mid-rapidity in proton-proton collisions are compared with those based on the similar transverse mass spectra measured in the most central beryllium-beryllium, argon-scandium and lead-lead collisions from the SPS at its BES energies.

Keywords: rapidity-dependent transverse momentum spectra, fine event patterns, three-dimensional space

PACS: 13.75.-n, 13.85.-t, 25.75.-q, 24.10.Pa

1 Introduction

The spectra of transverse momentum and (pseudo)rapidity of particles produced in high energy collisions are of high interest as soon as they provide us with an important information of the kinetic freeze-out state of the interacting system. The transverse momentum spectrum, characterizing the system developments in the transverse plane, is associated either with the effective temperature or with the freeze-out temperature, where the first contains contributions of thermal motion and flow effect, while the latter is believed to get the contribution of the thermal motion only. The rapidity spectrum characterizes the system development in the longitudinal direction and allows extracting such an important feature of the system as the rapidity shift and the width of the distribution. In the center-of-mass energy, ranging from a few GeV to above ten TeV, the highest nowadays collision energy available [1–4], the changing features of the transverse momentum and rapidity spectra bring crucial information about the changes in the particle production process.

To describe the transverse momentum and rapidity spectra, one can use different distributions under the assumption of isotropic emission in the transverse plane and consider rapidity shift in the longitudinal direction. The distributions for transverse momentum spectrum include, but are not limited to, the standard (Fermi-Dirac, Bose-Einstein and Boltzmann) distribution [5–8], Tsallis distribution [8–15], Erlang distribution [15], inverse power-law [16–18], Schwinger mechanism [19–22], exponential function and blast-wave model [23–26]. In some cases, one distribution has different forms or revisions. The distributions for rapidity spectrum includes mainly Gaussian [27–37], double-Gaussian and multi-Gaussian functions [38–40], as well as Gaussian-like functional forms. From a few GeV to above ten TeV, it is expected that the interacting system undergoes different phase states and has different reaction mechanisms. One can use different distributions or the same distribution with different parameter values to describe the different spectra.

Based on the descriptions of transverse momentum and rapidity spectra, one can structure event patterns by using scatter plots of identified particles at the stage of kinetic freeze-out of interacting system. Our previous works [41–43] show that different kinds of particles present different scatter plots thus different event patterns. In particular, the event patterns displayed by the scatter plots of light and heavy flavor particles in

*E-mail: fuhuliu@163.com; fuhuliu@sxu.edu.cn

†E-mail: Edward.Sarkisyan-Grinbaum@cern.ch

three-dimensional velocity space are spherical and cylindrical respectively, which show an obvious difference in the shape and reflect different production mechanisms or stages. In addition, if we consider the effects of non-zero elliptic flow on the two spectra, more accurate event patterns can be obtained [44]. However, the effects of non-zero elliptic flow on the two spectra and event patterns are in fact very small. One can neglect non-zero elliptic flow in the case of describing the two spectra and structuring the event patterns.

In most cases, the transverse momentum spectra are measured at mid-rapidity or in the vicinity of a given rapidity only. These spectra then often applied at other rapidities which leads to the rapidity-independent spectra. These spectra have been used in our previous works [41–44] leading to the event patterns being non-fine in this sense. Here, we are interested in the use of the rapidity-dependent spectra measured at different rapidities so structuring the fine event patterns. For a not wide transverse momentum spectrum (less than of $\sim$ 2–3 GeV), one can use either the standard distribution or the one combining two standard distributions ("two-component standard distribution") with different parameter values to describe the rapidity-dependent spectra. In the distributions, the chemical potential and spin property of considered particles can be included if the collision energy per nucleon in center-of-mass system is not too high (less than dozens of GeV). Generally, rapidity spectrum can be described by Gaussian, double-Gaussian, or even three-Gaussian distribution in our studies.

In this paper, rapidity-dependent double-differential transverse momentum spectra of negatively charged pions (π^-) measured at different rapidities and rapidity spectra of π^- produced in proton-proton (pp) collisions at the Super Proton Synchrotron (SPS) at its Beam Energy Scan (BES) energies are investigated. Related parameters are extracted by fitting the experimental data of the NA61/SHINE Collaboration [45] and fine event patterns in pp collisions are structured by fine scatter plots of π^- due to rapidity-dependent spectra being used. As a comparison, non-fine results extracted from the experimental transverse mass spectra at mid-rapidity and rapidity spectra of π^- produced in pp collisions and central (0–5%) beryllium-beryllium (Be-Be), argon-scandium (Ar-Sc), as well as lead-lead (Pb-Pb) collisions at the SPS at its BES energies [46–50] are presented, where the transverse mass spectra at mid-rapidity are used for whole rapidity range. The transverse mass spectra used in the present work are rapidity-independent.

2 The model and method

As what we did in our recent work [44], first of all, we structure a right-handed coordinate system and definite some variables before introducing the model and method. Let the collision point be the original O, one of the beam directions be the Oz axis and the reaction plane be the xOz plane. Thus, the transverse plane is the xOy plane, the Ox axis is along the impact parameter and the Oy axis is perpendicular to the xOz plane. Further, the velocity (momentum) components on the Ox, Oy and Oz axes are denoted by β_x, β_y and β_z (p_x, p_y and p_z), respectively. According to rapidity Y defined generally by energy E and p_z, one can define rapidity Y_1 by E and p_x, as well as rapidity Y_2 by E and p_y. Finally, the three-dimensional velocity (β_x-β_y-β_z), momentum (p_x-p_y-p_z) and rapidity (Y_1-Y_2-Y) spaces are structured by us.

The model used in the present work is in fact a hybrid model. In consideration of different functions in descriptions of transverse momentum ($p_{\rm T}$) or transverse mass ($m_{\rm T}$) spectra of particles produced in soft process, we choose the standard distribution and its superposition if necessary. In description of Y spectrum of particles, we choose a double-Gaussian function. The center-of-mass energy range focused on in the present work is from 6.1 (6.3) to 16.8 (17.3) GeV which is the SPS at its BES energies. In this energy range, the chemical potential and spin property of considered particles are included in our treatment on soft excitation process, and the contribution of hard scattering process can be neglected due to its nearly zero fraction.

The standard distribution has more than one forms. In the case of considering $p_{\rm T}$ spectrum, we choose the probability density function [8]

$$f_{p_{\rm T}}(p_{\rm T},T)=\frac{1}{N}\frac{dN}{dp_{\rm T}}=Cp_{\rm T}m_{\rm T}\int_{Y_{\min}}^{Y_{\max}}\cosh Y \times\left[\exp\left(\frac{m_{\rm T}\cosh Y-\mu}{T}\right)+S\right]^{-1}dY, \tag{1}$$

where N denotes the number of particles, C denotes the normalization constant, $m_{\rm T}=\sqrt{p_{\rm T}^2+m_0^2}$ and m_0 is the rest mass, $Y_{\min}$ is the minimum Y and $Y_{\max}$ is the maximum Y in the case of shifting the mid-value of Y to 0, μ is the chemical potential, T is the effective temperature and $S=+1$ and -1 correspond to fermions and bosons respectively. In particular, $S=+1$, -1 and 0 also correspond to Fermi-Dirac, Bose-Einstein and Boltzmann statistics, respectively. In the case of considering $m_{\rm T}$

spectrum, we have the normalized standard distribution

$$f_{m_\mathrm{T}}(m_\mathrm{T},T) = \frac{1}{N}\frac{dN}{dm_\mathrm{T}} = Cm_\mathrm{T}^2\int_{Y_\mathrm{min}}^{Y_\mathrm{max}} \cosh Y \times \left[\exp\left(\frac{m_\mathrm{T}\cosh Y-\mu}{T}\right)+S\right]^{-1} dY. \quad (2)$$

Because of the similarity between expressions of $f_{p_\mathrm{T}}(p_\mathrm{T},T)$ and $f_{m_\mathrm{T}}(m_\mathrm{T},T)$, one can use directly parameters obtained from one function to another one. For wide p_T (m_T) spectrum, a single standard distribution may not fit the data simultaneously in the low-p_T and high-p_T regions. This would require a combination of two or three standard distributions given the spectrum width. In the case of using the two-component standard distribution, we have to use two effective temperatures, T_1 and T_2, for the first and second components respectively. Meanwhile, one relative fraction, k_1, for the first component is needed. The two-component standard distribution is written to be

$$f_{p_\mathrm{T}}(p_\mathrm{T}) = k_1 f_{p_\mathrm{T}}(p_\mathrm{T},T_1)+(1-k_1)f_{p_\mathrm{T}}(p_\mathrm{T},T_2) \quad (3)$$

for p_T spectrum, or

$$f_{m_\mathrm{T}}(m_\mathrm{T}) = k_1 f_{m_\mathrm{T}}(m_\mathrm{T},T_1)+(1-k_1)f_{m_\mathrm{T}}(m_\mathrm{T},T_2) \quad (4)$$

for m_T spectrum. The effective temperature of interacting system is then obtained by $T = k_1T_1 + (1-k_1)T_2$. Generally, two-component standard distribution is enough to describe particle spectra in soft process. Three- or multi-standard distribution is not necessary.

In the above functions, μ should not be regarded as a free parameter due to its insensitivity to p_T or m_T spectrum. Instead, μ for particle type i, denoted by μ_i, can be obtained from the ratio of negatively to positively charged particles. The following expression for μ_i

$$\mu_i = -\frac{1}{2}T_\mathrm{ch}\ln(k_i), \quad (5)$$

is applied, which is shown [51] to well reproduce the ratio of negatively to positively charged particles (k_i) relating it with the chemical freeze-out temperature T_ch within the thermal model [52]. A relation between the yield (n) and the mass (m) obtained in [53, 54], leads to the ratio of the first to the second particles:

$$\frac{n_1}{n_2} = \frac{\exp(m_2/T_\mathrm{ch})+S_2}{\exp(m_1/T_\mathrm{ch})+S_1}, \quad (6)$$

where $S_1(S_2) = \pm1$ denote fermions and bosons respectively. In central nucleus-nucleus collisions, an empirical expression for T_ch is applied [55–58]:

$$T_\mathrm{ch} = 0.164\left\{1+\exp\left[2.60-\frac{\ln(\sqrt{s_\mathrm{NN}})}{0.45}\right]\right\}^{-1}, \quad (7)$$

where $\sqrt{s_\mathrm{NN}}$ is the center-of-mass energy. Both the units of T_ch and $\sqrt{s_\mathrm{NN}}$ in Eq. (7) are in GeV, though T_ch and other temperatures appear in the units of MeV in many cases.

For Y spectrum, one can use the normalized symmetrical double-Gaussian function as used by the NA61/SHINE [45] and NA49 Collaborations [47, 48]. That is,

$$f_Y(Y) = \frac{1}{2\sqrt{2\pi}\sigma_Y}\left\{\exp\left[-\frac{(Y+\delta Y)^2}{2\sigma_Y^2}\right] + \exp\left[-\frac{(Y-\delta Y)^2}{2\sigma_Y^2}\right]\right\}, \quad (8)$$

where δY and σ_Y denote the rapidity shift and distribution width respectively. In the case of considering asymmetrical double-Gaussian function, we have to introduce the relative fraction of the first (or second) component. Meanwhile, the rapidity shifts and distribution widths for the two components are separately different from each other. The present work focuses on symmetrical or approximately symmetrical collisions. Eq. (8) is an appropriate treatment that is acceptable for us.

The Monte Carlo distribution generating method is used below to obtain p_T and m_T sampled according to the above functions $f_{p_\mathrm{T}}(p_\mathrm{T})$ and $f_{m_\mathrm{T}}(m_\mathrm{T})$. Let R denotes the random number distributed evenly in $[0,1]$. The values of p_T can be obtained by

$$\int_0^{p_\mathrm{T}} f_{p_\mathrm{T}}(p'_\mathrm{T})dp'_\mathrm{T} < R < \int_0^{p_\mathrm{T}+\delta p_\mathrm{T}} f_{p_\mathrm{T}}(p'_\mathrm{T})dp'_\mathrm{T}, \quad (9)$$

or, the values of m_T can be obtained by

$$\int_{m_0}^{m_\mathrm{T}} f_{m_\mathrm{T}}(m'_\mathrm{T})dm'_\mathrm{T} < R < \int_{m_0}^{m_\mathrm{T}+\delta m_\mathrm{T}} f_{m_\mathrm{T}}(m'_\mathrm{T})dm'_\mathrm{T}, \quad (10)$$

where δp_T and δm_T denote small shifts relative to p_T and m_T, respectively. Our initial target is to obtain p_T. In the case of obtaining m_T, we have $p_\mathrm{T} = \sqrt{m_\mathrm{T}^2 - m_0^2}$.

Under the assumption of isotropic emission in the transverse plane, we have

$$p_x = p_\mathrm{T}\cos\varphi = p_\mathrm{T}\cos(2\pi R_0) \quad (11)$$

and

$$p_y = p_\mathrm{T}\sin\varphi = p_\mathrm{T}\sin(2\pi R_0) \quad (12)$$

respectively, where

$$\varphi = \arctan\left(\frac{p_y}{p_x}\right) = 2\pi R_0 \quad (13)$$

denotes the azimuthal angle and R_0 denotes the random number distributed evenly in $[0,1]$. Because of the assumption of isotropic emission in the transverse plane,

p_x and p_y do not result in non-zero elliptic flow. As mentioned in the above section, the effects of non-zero elliptic flow on $p_{\rm T}$ spectra, Y spectra and scatter plots of particles are very small and can be actually neglected [44]. Our assumption of isotropic emission in the transverse plane is acceptable.

In the Monte Carlo method for the double-Gaussian function for Y spectrum, let $R_{1,2}$ denote the random numbers distributed evenly in $[0,1]$. We have

$$Y = \sigma_Y \sqrt{-2\ln R_1}\cos(2\pi R_2) - \delta Y \qquad (14)$$

in the calculation due to Y expressed as above obeying Gaussian function and the first component being Gaussian and similarly for the second component. The $\cos(2\pi R_2)$ in the above expression can be replaced by $\sin(2\pi R_2)$ [59]. In symmetrical collisions, the two components have the same relative fraction, i.e. 0.5. According to Y, we have

$$p_z = m_{\rm T} \sinh Y \qquad (15)$$

and

$$E = \sqrt{p_z^2 + m_{\rm T}^2}. \qquad (16)$$

Further,

$$\beta_x = \frac{p_x}{E}, \qquad (17)$$

$$\beta_y = \frac{p_y}{E}, \qquad (18)$$

$$\beta_z = \frac{p_z}{E}, \qquad (19)$$

$$Y_1 \equiv \frac{1}{2}\ln\left(\frac{E+p_x}{E-p_x}\right), \qquad (20)$$

$$Y_2 \equiv \frac{1}{2}\ln\left(\frac{E+p_y}{E-p_y}\right). \qquad (21)$$

So far, the expressions of components in three-dimensional β_x-β_y-β_z, p_x-p_y-p_z and Y_1-Y_2-Y spaces are obtained.

The step-by-step calculations are made below, from Eq. (3) to Eqs. (17–21), to obtain the event patterns in the three-dimensional β_x-β_y-β_z, p_x-p_y-p_z and Y_1-Y_2-Y plots.

3 Results and discussion

Figure 1 shows the rapidity-dependent $p_{\rm T}$ spectra, $(d^2n)/(dYdp_{\rm T})$, of π^- at different rapidities produced in pp collisions at beam momentum $p_{\rm beam}$ = (a) 20, (b) 31, (c) 40, (d) 80 and (e) 158 GeV/c which correspond to $\sqrt{s_{\rm NN}}$ = 6.3, 7.7, 8.8, 12.3 and 17.3 GeV, respectively, where n denote the number of π^-. The symbols represent the experimental data of the NA61/SHINE Collaboration [45] measured at different Y and scaled by different amounts marked in the last panel. The curves are the fits of standard (or two-component standard) distribution. In the calculations, to obtain correct values of parameters, we have to shift Y to 0 and use $Y_{\rm min} = -0.1$ and $Y_{\rm max} = 0.1$ for each case. At different $p_{\rm beam}$ and $\sqrt{s_{\rm NN}}$, the values of μ_π in pp collisions, based on Eqs. (5) and (6) and ref. [60] where n_K and n_π are available to read out from a table, are listed in Table 1 with n_K/n_π. The values of free parameters (T_1, T_2 and k_1), derivative parameter (T), normalization constant ($N_{p_{\rm T}}$), as well as χ^2 and degree of freedom (dof) in terms of χ^2/dof are listed in Table 2. One can see that the (two-component) standard distribution describes well the NA61/SHINE experimental $p_{\rm T}$ spectra of π^- measured at different Y in pp collisions at the SPS at its BES energies. With increasing Y and $\sqrt{s_{\rm NN}}$, the parameters show some features discussed below.

Figure 2 shows the $m_{\rm T}$ spectra, $1/m_{\rm T} \cdot (d^2n)/(dYdm_{\rm T})$, of π^- at mid-rapidity (0–0.2) produced in pp collisions at $p_{\rm beam}$ = (a) 20, (b) 31, (c) 40, (d) 80 and (e) 158 GeV/c, in central (0–5%) ^{7}Be-^{9}Be (Be-Be) collisions at (a) 20, (b) 30, (c) 40, (d) 75 and (e) 150 GeV/c, in central (0–5%) Ar-Sc collisions at (a) 19, (b) 30, (c) 40, (d) 75 and (e) 150 GeV/c, and in central (0–5%) Pb-Pb collisions at (a) 20, (b) 30, (c) 40, (d) 80 and (e) 158 GeV/c. The values of $\sqrt{s_{\rm NN}}$ corresponding to $p_{\rm beam}$ = 19, 30, 75 and 150 GeV/c are 6.1, 7.6, 11.9 and 16.8 GeV, respectively, where the relations for other $\sqrt{s_{\rm NN}}$ and $p_{\rm beam}$ as given just above and the asymmetries in ^{7}Be-^{9}Be and Ar-Sc collisions are neglected. The symbols represent the experimental data of the NA61/SHINE [46] and NA49 Collaborations [47, 48]. The curves are the fits of (two-component) standard distribution. The values of μ_π and k_π in central Pb-Pb collisions, based on Eqs. (5) and (7) and ref. [61] where k_π is available to read out from a plot, are listed in Table 1. The values of μ_π in central Be-Be and Ar-Sc collisions are taken to be 0 due to k_π being not available and μ_π having small effect on π spectra. The values of T_1, T_2, k_1, T, normalization constant ($N_{m_{\rm T}}$) and χ^2/dof are listed in Table 3. One can see that the (two-component) standard distribution describes well the NA61/SHINE and NA49 experimental $m_{\rm T}$ spectra of π^- measured in different collisions at the SPS at its BES energies. With increasing system size (A) and $\sqrt{s_{\rm NN}}$, where A denotes the total nucleon number of projectile and target nuclei, the parameters show some features discussed below.

Figure 3 shows the Y spectra, dn/dY, of π^- produced in (a) pp, (b) central Be-Be, (c) central Ar-Sc [45, 49, 50] and (d) central Pb-Pb collisions [47, 48] at

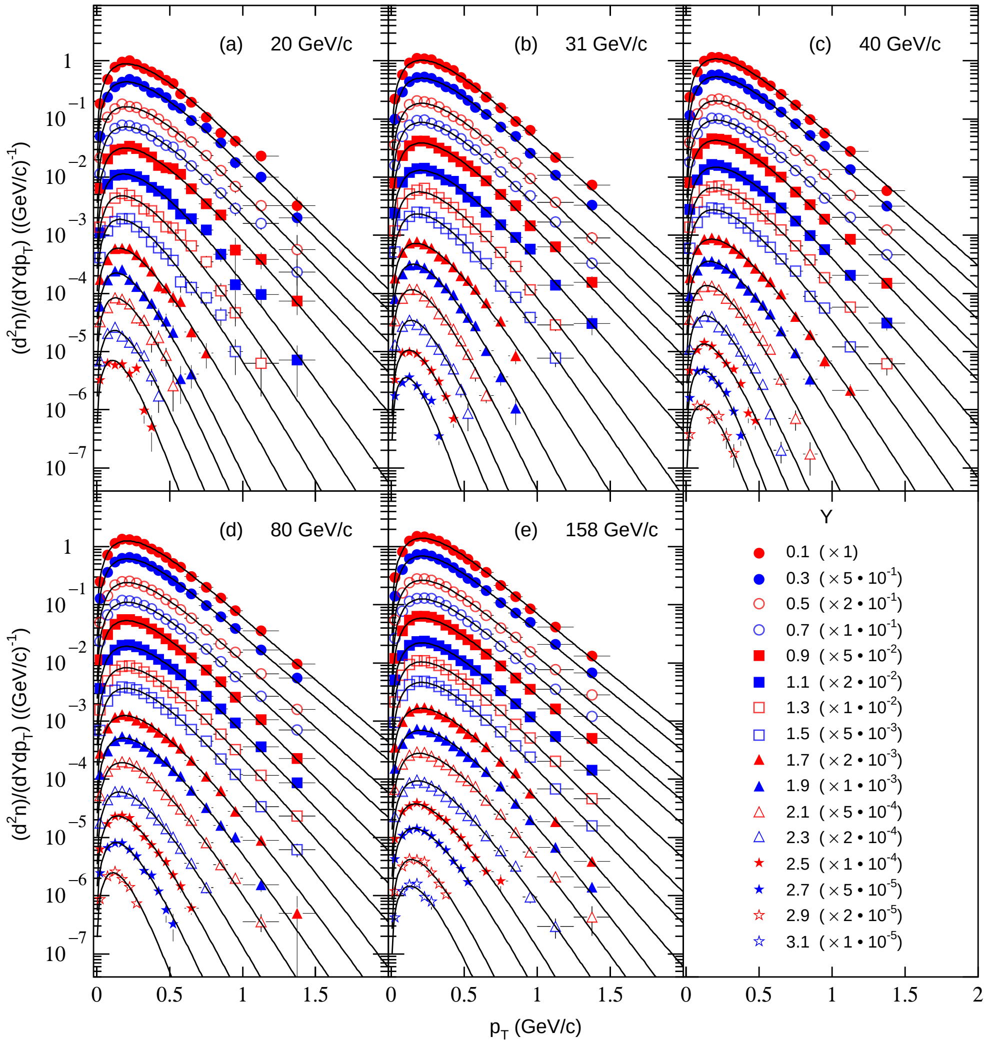

Fig. 1. (color online) Rapidity-dependent double-differential transverse momentum spectra of π^- at different rapidities Y (rapidity bin centers) produced in pp collisions at (a) 20, (b) 31, (c) 40, (d) 80 and (e) 158 GeV/c. The symbols represent the experimental data of the NA61/SHINE Collaboration [45] and the curves are the fits of (two-component) standard distribution. The parameters are listed in Table 2.

five momenta with little variations marked in the panels. The values of $\sqrt{s_{\rm NN}}$ corresponding to different momenta are given in the just above. The closed symbols represent the experimental data of the NA61/SHINE [45, 49, 50] and NA49 Collaborations [47, 48] and the open ones are reflected at $y = 0$ [45, 47–50]. The curves are the fits of double-Gaussian functions performed in refs. [45, 47, 48] for pp and central Pb-Pb collisions or by us for central Be-Be and Ar-Sc collisions. The values of free parameters (δY and σ_Y) and normalization constant (N_Y) used in refs. [45, 47, 48] for pp and central Pb-Pb collisions or by us for central Be-Be and Ar-Sc collisions, as well as χ^2/dof are listed in Table 4. One can see that the double-Gaussian function describes well the NA61/SHINE and NA49 experimental Y spectra of π^- measured in different collisions at the SPS at its BES energies. With increasing A and $\sqrt{s_{\rm NN}}$, the parameters show some features discussed below.

According to the parameter values obtained from Figs. 1 and 3 (or similarly Figs. 2 and 3) and listed in Tables 2 and 4 (Tables 3 and 4), the Monte Carlo calculation can be performed and a series of values of some kinematical quantities can be obtained. According to these kinematical quantities, some scatter plots of π^- at the kinetic freeze-out can be structured. These scatter plots are in fact the event patterns at the last stage of collision process in the interacting system. Some characteristic examples of the scatter plots are shown in Figs. 4 to 6.

Figure 4 shows a few scatter plots in pp and nucleus-

Table 1. Values of $T_{\rm ch}$ and μ_π obtained from Eqs. (5) and (6) (or (7)) in pp (or central Pb-Pb) collisions at different $\sqrt{s_{\rm NN}}$ with different n_K/n_π (or k_π) read out from a table (or plot) in ref. [60] (or [61]).

Type	$\sqrt{s_{\rm NN}}$/GeV	$T_{\rm ch}$/MeV	μ_π/MeV	n_K/n_π (or k_π)
pp	6.3	126 ± 3	34.8 ± 21.0	0.574 ± 0.205
	7.7	147 ± 3	25.3 ± 19.3	0.708 ± 0.203
	8.8	153 ± 4	25.6 ± 15.1	0.716 ± 0.149
	12.3	155 ± 4	21.3 ± 12.6	0.760 ± 0.129
	17.3	160 ± 4	20.5 ± 14.6	0.773 ± 0.155
Central Pb-Pb	6.3	134 ± 3	-10.3 ± 4.8	1.166 ± 0.086
	7.6	142 ± 3	-7.6 ± 6.8	1.112 ± 0.140
	8.8	148 ± 4	-5.6 ± 8.4	1.092 ± 0.147
	12.3	156 ± 4	-5.1 ± 3.8	1.067 ± 0.074
	17.3	160 ± 4	-2.4 ± 5.0	1.031 ± 0.086

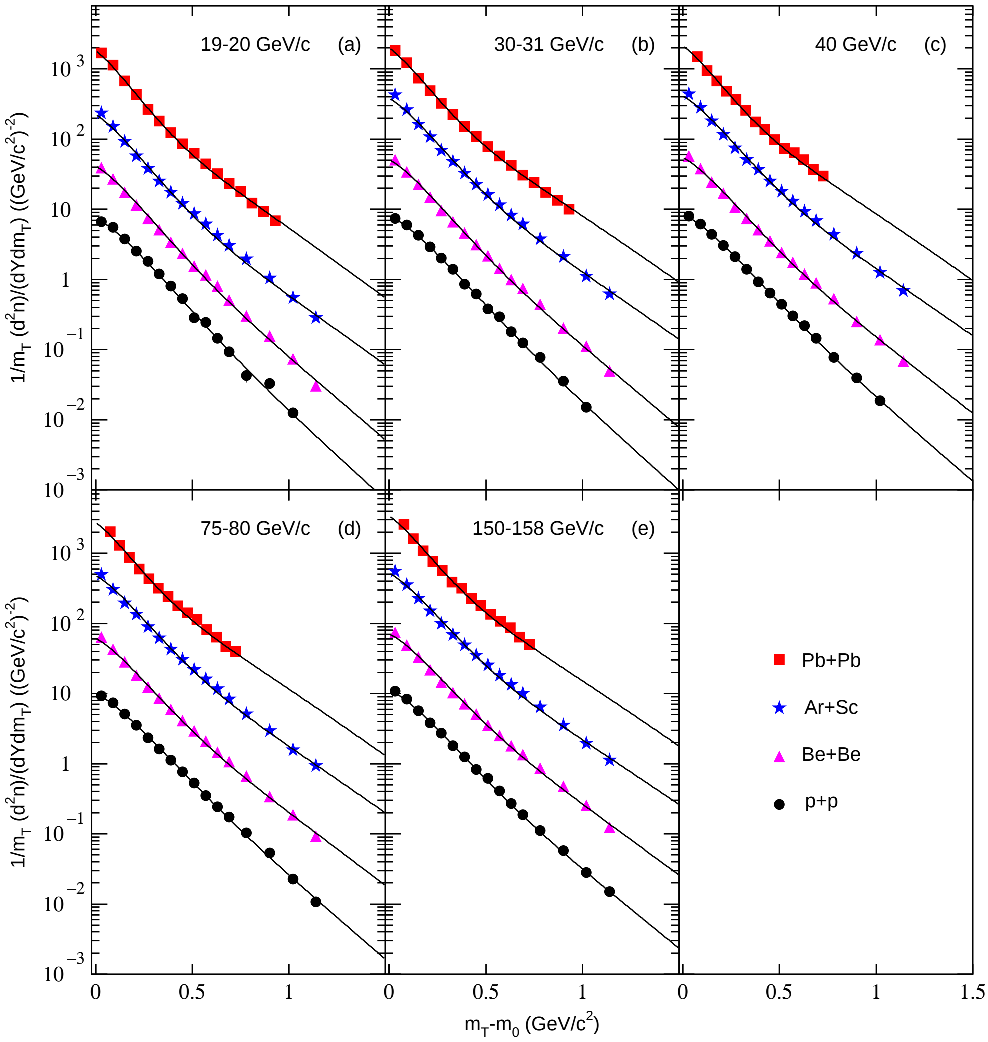

Fig. 2. (color online) Double-differential transverse mass spectra of π^- at mid-rapidity (0–0.2) produced in pp collisions at (a) 20, (b) 31, (c) 40, (d) 80 and (e) 158 GeV/c [46], in central Be-Be collisions at (a) 20, (b) 30, (c) 40, (d) 75 and (e) 150 GeV/c [46], in central Ar-Sc collisions at (a) 19, (b) 30, (c) 40, (d) 75 and (e) 150 GeV/c [46], and in central Pb-Pb collisions at (a) 20, (b) 30, (c) 40, (d) 80 and (e) 158 GeV/c [47, 48]. The symbols represent the experimental data of the NA61/SHINE [46] and NA49 Collaborations [47, 48] and the curves are the fits of (two-component) standard distribution. The parameters are listed in Table 3.

Table 2. Values of free parameters (T_1, T_2 and k_1), derivative parameter (T), normalization constant (N_{p_T}) and χ^2/dof for the curves fitted the rapidity-dependent p_T spectra in Fig. 1.

$\sqrt{s_{\mathrm{NN}}}$/GeV	Y	T_1/MeV	T_2/MeV	k_1	T/MeV	N_{p_T}	χ^2/dof
6.3	0.0 − 0.2	115 ± 2	154 ± 3	0.78 ± 0.02	124 ± 2	0.41 ± 0.02	12/14
	0.2 − 0.4	115 ± 2	154 ± 3	0.78 ± 0.02	124 ± 2	0.40 ± 0.02	20/14
	0.4 − 0.6	115 ± 2	150 ± 3	0.80 ± 0.02	122 ± 2	0.37 ± 0.02	12/14
	0.6 − 0.8	115 ± 2	147 ± 2	0.85 ± 0.02	120 ± 2	0.33 ± 0.02	10/14
	0.8 − 1.0	115 ± 2	140 ± 2	0.92 ± 0.02	117 ± 2	0.28 ± 0.01	11/14
	1.0 − 1.2	107 ± 2	−	1.00 ± 0.00	107 ± 2	0.23 ± 0.01	21/16
	1.2 − 1.4	98 ± 2	−	1.00 ± 0.00	98 ± 2	0.18 ± 0.01	17/15
	1.4 − 1.6	90 ± 2	−	1.00 ± 0.00	90 ± 2	0.13 ± 0.01	10/14
	1.6 − 1.8	82 ± 2	−	1.00 ± 0.00	82 ± 2	0.10 ± 0.01	8/12
	1.8 − 2.0	71 ± 1	−	1.00 ± 0.00	71 ± 1	0.06 ± 0.01	12/11
	2.0 − 2.2	66 ± 1	−	1.00 ± 0.00	66 ± 1	0.04 ± 0.01	6/9
	2.2 − 2.4	60 ± 1	−	1.00 ± 0.00	60 ± 1	0.03 ± 0.01	3/7
	2.4 − 2.6	51 ± 1	−	1.00 ± 0.00	51 ± 1	0.02 ± 0.01	8/6
7.7	0.0 − 0.2	115 ± 2	164 ± 3	0.77 ± 0.02	126 ± 2	0.48 ± 0.02	16/14
	0.2 − 0.4	115 ± 2	159 ± 3	0.77 ± 0.02	125 ± 2	0.47 ± 0.02	11/14
	0.4 − 0.6	115 ± 2	154 ± 3	0.78 ± 0.02	124 ± 2	0.43 ± 0.02	16/14
	0.6 − 0.8	115 ± 2	151 ± 3	0.80 ± 0.02	122 ± 2	0.40 ± 0.02	14/14
	0.8 − 1.0	115 ± 2	147 ± 2	0.83 ± 0.02	120 ± 2	0.35 ± 0.02	10/14
	1.0 − 1.2	115 ± 2	143 ± 2	0.92 ± 0.02	117 ± 2	0.29 ± 0.01	18/14
	1.2 − 1.4	108 ± 2	−	1.00 ± 0.00	108 ± 2	0.23 ± 0.01	15/15
	1.4 − 1.6	101 ± 2	−	1.00 ± 0.00	101 ± 2	0.18 ± 0.01	11/15
	1.6 − 1.8	93 ± 2	−	1.00 ± 0.00	93 ± 2	0.13 ± 0.01	12/13
	1.8 − 2.0	79 ± 2	−	1.00 ± 0.00	79 ± 2	0.10 ± 0.01	10/13
	2.0 − 2.2	71 ± 1	−	1.00 ± 0.00	71 ± 1	0.07 ± 0.01	8/11
	2.2 − 2.4	62 ± 1	−	1.00 ± 0.00	62 ± 1	0.04 ± 0.01	5/9
	2.4 − 2.6	58 ± 1	−	1.00 ± 0.00	58 ± 1	0.03 ± 0.01	3/7
	2.6 − 2.8	46 ± 1	−	1.00 ± 0.00	46 ± 1	0.01 + 0.01	7/5
8.8	0.0 − 0.2	115 ± 2	167 ± 3	0.76 ± 0.02	127 ± 2	0.51 ± 0.03	23/14
	0.2 − 0.4	115 ± 2	163 ± 3	0.77 ± 0.02	126 ± 2	0.50 ± 0.03	19/14
	0.4 − 0.6	115 ± 2	159 ± 3	0.77 ± 0.02	125 ± 2	0.48 ± 0.02	30/14
	0.6 − 0.8	115 ± 2	153 ± 3	0.78 ± 0.02	123 ± 2	0.44 ± 0.02	24/14
	0.8 − 1.0	115 ± 2	148 ± 2	0.82 ± 0.02	121 ± 2	0.39 ± 0.02	26/14
	1.0 − 1.2	115 ± 2	140 ± 2	0.88 ± 0.02	118 ± 2	0.33 ± 0.02	24/14
	1.2 − 1.4	112 ± 2	−	1.00 ± 0.00	112 ± 2	0.28 ± 0.01	23/16
	1.4 − 1.6	105 ± 2	−	1.00 ± 0.00	105 ± 2	0.22 ± 0.01	23/15
	1.6 − 1.8	97 ± 2	−	1.00 ± 0.00	97 ± 2	0.16 ± 0.01	14/15
	1.8 − 2.0	87 ± 2	−	1.00 ± 0.00	87 ± 2	0.12 ± 0.01	8/13
	2.0 − 2.2	74 ± 1	−	1.00 ± 0.00	74 ± 1	0.08 ± 0.01	45/13
	2.2 − 2.4	65 ± 1	−	1.00 ± 0.00	65 ± 1	0.05 ± 0.01	42/11
	2.4 − 2.6	60 ± 1	−	1.00 ± 0.00	60 ± 1	0.03 ± 0.01	11/8
	2.6 − 2.8	52 ± 1	−	1.00 ± 0.00	52 ± 1	0.02 ± 0.01	7/6
	2.8 − 3.0	48 ± 1	−	1.00 ± 0.00	48 ± 1	0.01 + 0.01	7/5
12.3	0.0 − 0.2	115 ± 2	170 ± 3	0.75 ± 0.02	129 ± 2	0.60 ± 0.03	19/14
	0.2 − 0.4	115 ± 2	170 ± 3	0.75 ± 0.02	129 ± 2	0.59 ± 0.03	15/14
	0.4 − 0.6	115 ± 2	164 ± 3	0.76 ± 0.02	127 ± 2	0.57 ± 0.03	14/14
	0.6 − 0.8	115 ± 2	161 ± 3	0.77 ± 0.02	126 ± 2	0.52 ± 0.03	12/14
	0.8 − 1.0	115 ± 2	154 ± 3	0.81 ± 0.02	122 ± 2	0.49 ± 0.02	16/14
	1.0 − 1.2	115 ± 2	150 ± 2	0.82 ± 0.02	121 ± 2	0.44 ± 0.02	21/14
	1.2 − 1.4	115 ± 2	142 ± 2	0.87 ± 0.02	119 ± 2	0.37 ± 0.02	19/14
	1.4 − 1.6	115 ± 2	−	1.00 ± 0.00	115 ± 2	0.32 ± 0.02	21/16
	1.6 − 1.8	110 ± 2	−	1.00 ± 0.00	110 ± 2	0.26 ± 0.01	18/16
	1.8 − 2.0	102 ± 2	−	1.00 ± 0.00	102 ± 2	0.20 ± 0.01	18/15
	2.0 − 2.2	94 ± 2	−	1.00 ± 0.00	94 ± 2	0.14 ± 0.01	9/15
	2.2 − 2.4	85 ± 2	−	1.00 ± 0.00	85 ± 2	0.10 ± 0.01	7/12
	2.4 − 2.6	75 ± 1	−	1.00 ± 0.00	75 ± 1	0.07 ± 0.01	11/11
	2.6 − 2.8	66 ± 1	−	1.00 ± 0.00	66 ± 1	0.04 ± 0.01	6/9
	2.8 − 3.0	53 ± 1	−	1.00 ± 0.00	53 ± 1	0.03 ± 0.01	3/4
17.3	0.0 − 0.2	115 ± 2	176 ± 3	0.76 ± 0.02	130 ± 2	0.67 ± 0.03	11/14
	0.2 − 0.4	115 ± 2	176 ± 3	0.76 ± 0.02	130 ± 2	0.66 ± 0.03	14/14
	0.4 − 0.6	115 ± 2	173 ± 3	0.76 ± 0.02	129 ± 2	0.63 ± 0.03	15/14
	0.6 − 0.8	115 ± 2	170 ± 3	0.76 ± 0.02	128 ± 2	0.60 ± 0.03	12/14
	0.8 − 1.0	115 ± 2	166 ± 3	0.75 ± 0.02	128 ± 2	0.56 ± 0.03	17/14
	1.0 − 1.2	115 ± 2	162 ± 3	0.76 ± 0.02	126 ± 2	0.52 ± 0.03	9/14
	1.2 − 1.4	115 ± 2	153 ± 3	0.80 ± 0.02	123 ± 2	0.48 ± 0.02	7/14
	1.4 − 1.6	115 ± 2	150 ± 2	0.85 ± 0.02	120 ± 2	0.42 ± 0.02	15/14
	1.6 − 1.8	115 ± 2	144 ± 2	0.93 ± 0.02	117 ± 2	0.37 ± 0.02	13/14
	1.8 − 2.0	114 ± 2	−	1.00 ± 0.00	114 ± 2	0.30 ± 0.02	8/16
	2.0 − 2.2	108 ± 2	−	1.00 ± 0.00	108 ± 2	0.23 ± 0.01	10/16
	2.2 − 2.4	100 ± 2	−	1.00 ± 0.00	100 ± 2	0.18 ± 0.01	11/15
	2.4 − 2.6	89 ± 2	−	1.00 ± 0.00	89 ± 2	0.13 ± 0.01	6/12
	2.6 − 2.8	81 ± 2	−	1.00 ± 0.00	81 ± 2	0.09 ± 0.01	2/9
	2.8 − 3.0	70 ± 1	−	1.00 ± 0.00	70 ± 1	0.06 ± 0.01	9/6
	3.0 − 3.2	63 ± 1	−	1.00 ± 0.00	63 ± 1	0.04 ± 0.01	12/4

Table 3. Values of T_1, T_2, k_1, T, normalization constant (N_{m_T}) and χ^2/dof for the curves fitted the m_T spectra in Fig. 2.

Type	$\sqrt{s_{NN}}$/GeV	T_1/MeV	T_2/MeV	k_1	T/MeV	N_{m_T}	χ^2/dof
pp	6.3	101 ± 2	161 ± 3	0.78 ± 0.02	114 ± 2	0.42 ± 0.02	10/10
	7.7	104 ± 2	164 ± 3	0.77 ± 0.02	118 ± 2	0.48 ± 0.02	4/10
	8.8	104 ± 2	169 ± 3	0.76 ± 0.02	120 ± 2	0.51 ± 0.03	3/10
	12.3	104 ± 2	169 ± 3	0.75 ± 0.02	120 ± 2	0.59 ± 0.03	4/11
	17.3	102 ± 2	177 ± 3	0.76 ± 0.02	120 ± 2	0.67 ± 0.03	3/11
Central Be-Be	6.3	94 ± 2	167 ± 3	0.75 ± 0.02	112 ± 2	2.1 ± 0.1	9/11
	7.6	95 ± 2	169 ± 3	0.73 ± 0.02	115 ± 2	2.7 ± 0.1	10/11
	8.8	97 ± 2	180 ± 3	0.74 ± 0.02	119 ± 2	3.0 ± 0.2	7/11
	11.9	96 ± 2	186 ± 3	0.72 ± 0.02	121 ± 2	3.4 ± 0.2	7/11
	16.8	98 ± 2	191 ± 3	0.72 ± 0.02	124 ± 2	4.1 ± 0.2	10/11
Central Ar-Sc	6.1	92 ± 2	193 ± 3	0.77 ± 0.02	115 ± 2	11 ± 1	7/11
	7.6	94 ± 2	199 ± 3	0.75 ± 0.02	120 ± 2	20 ± 1	8/11
	8.8	95 ± 2	200 ± 3	0.75 ± 0.02	121 ± 2	22 ± 1	12/11
	11.9	95 ± 2	201 ± 3	0.74 ± 0.02	123 ± 2	26 ± 1	9/11
	16.8	96 ± 2	206 ± 3	0.73 ± 0.02	126 ± 2	29 ± 1	8/11
Central Pb-Pb	6.3	83 ± 2	190 ± 3	0.69 ± 0.02	116 ± 2	81 ± 4	92/11
	7.6	85 ± 2	199 ± 3	0.66 ± 0.02	124 ± 2	96 ± 5	70/11
	8.8	84 ± 2	198 ± 3	0.65 ± 0.02	124 ± 2	102 ± 5	79/9
	12.3	84 ± 2	198 ± 3	0.64 ± 0.02	125 ± 2	133 ± 6	102/9
	17.3	86 ± 2	202 ± 3	0.65 ± 0.02	127 ± 2	169 ± 8	93/9

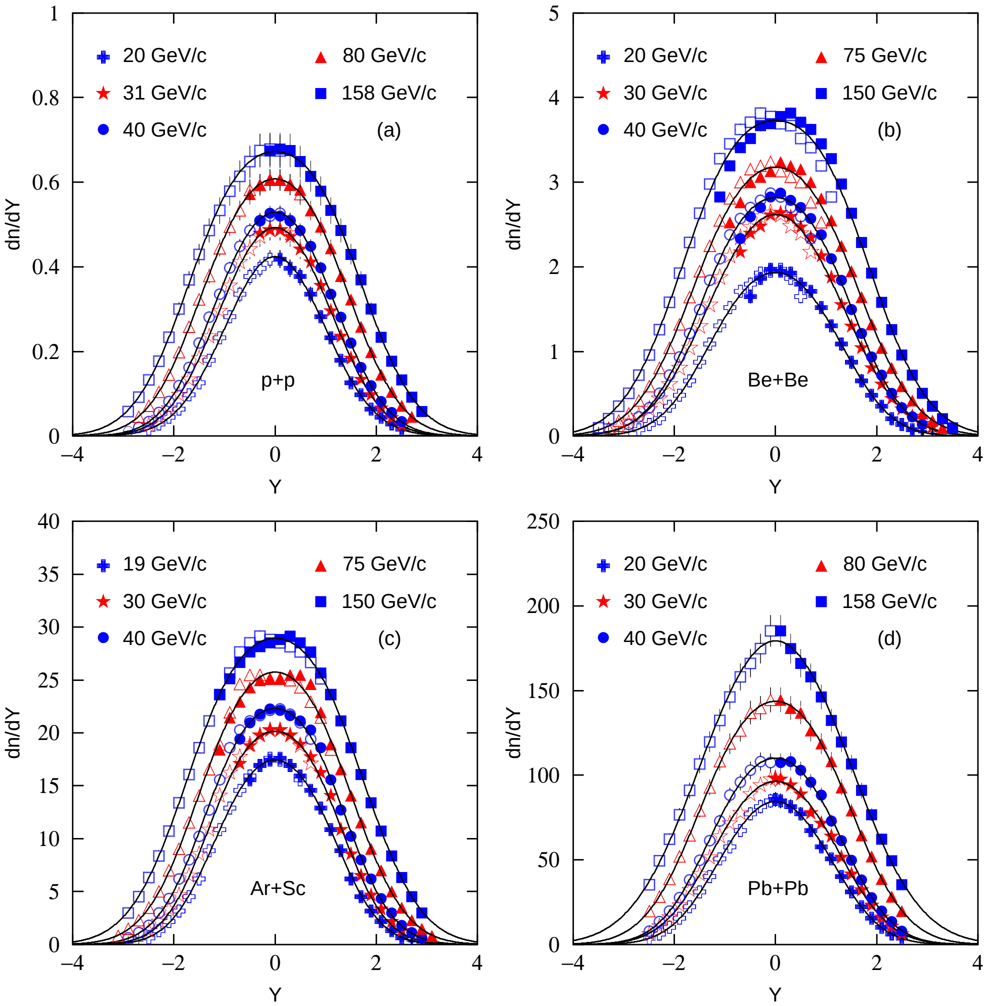

Fig. 3. (color online) Rapidity spectra of π^- produced in (a) pp, (b) central Be-Be, (c) central Ar-Sc [45, 49, 50] and (d) central Pb-Pb collisions [47, 48] at different momenta marked in the panels. The closed symbols represent the experimental data of the NA61/SHINE [45, 49, 50] and NA49 Collaborations [47, 48] and the open ones are reflected at $y = 0$ [45, 47–50]. The curves are the fits of double-Gaussian functions performed in refs. [45, 47, 48] for pp and central Pb-Pb collisions or by us for central Be-Be and Ar-Sc collisions. The fit parameters are given in Table 4.

Table 4. Values of free parameters (δY and σ_Y) and normalization constant (N_Y) used in refs. [45, 47, 48] for pp and central Pb-Pb collisions or by us for central Be-Be and Ar-Sc collisions, as well as χ^2/dof for the curves in Fig. 3.

Type	$\sqrt{s_{\rm NN}}$/GeV	δY	σ_Y	N_Y	χ^2/dof
pp	6.3	0.337 ± 0.046	0.921 ± 0.118	1.05 ± 0.05	2/10
	7.7	0.545 ± 0.055	0.875 ± 0.050	1.31 ± 0.07	2/13
	8.8	0.604 ± 0.044	0.882 ± 0.045	1.48 ± 0.05	5/14
	12.3	0.733 ± 0.010	0.937 ± 0.019	1.94 ± 0.08	1/14
	17.3	0.860 ± 0.021	1.007 ± 0.051	2.44 ± 0.13	2/13
Central Be-Be	6.3	0.659 ± 0.033	0.875 ± 0.044	5.6 ± 0.05	6/16
	7.6	0.664 ± 0.033	1.006 ± 0.050	8.2 ± 0.07	8/18
	8.8	0.753 ± 0.038	0.934 ± 0.046	9.1 ± 0.05	10/18
	11.9	0.826 ± 0.041	1.026 ± 0.050	11.3 ± 0.08	27/20
	16.8	0.938 ± 0.047	1.080 ± 0.050	14.7 ± 0.13	59/21
Central Ar-Sc	6.1	0.605 ± 0.030	0.795 ± 0.035	46 ± 2	2/15
	7.6	0.663 ± 0.033	0.810 ± 0.040	57 ± 3	6/16
	8.8	0.701 ± 0.035	0.859 ± 0.042	67 ± 3	7/16
	11.9	0.764 ± 0.038	0.953 ± 0.047	85 ± 4	23/19
	16.8	0.879 ± 0.043	1.042 ± 0.050	108 ± 5	8/18
Central Pb-Pb	6.3	0.557 ± 0.009	0.837 ± 0.007	221 ± 12	2/11
	7.6	0.624 ± 0.009	0.885 ± 0.007	274 ± 15	3/11
	8.8	0.666 ± 0.006	0.872 ± 0.005	322 ± 19	2/10
	12.3	0.756 ± 0.006	0.974 ± 0.007	474 ± 28	1/10
	17.3	0.720 ± 0.020	1.180 ± 0.020	639 ± 48	3/10

nucleus collisions in β_x-β_y-β_z space. The values of root-mean-squares $\sqrt{\overline{\beta_x^2}}$ for β_x, $\sqrt{\overline{\beta_y^2}}$ for β_y and $\sqrt{\overline{\beta_z^2}}$ for β_z, as well as the maximum $|\beta_x|$, $|\beta_y|$ and $|\beta_z|$ (i.e. $|\beta_x|_{\rm max}$, $|\beta_y|_{\rm max}$ and $|\beta_z|_{\rm max}$) for various systems and energies are listed in Table 5. One can see that both the event patterns in β_x-β_y-β_z space obtained from the rapidity-dependent and rapidity-independent spectra in pp collisions are spherical, though $\sqrt{\overline{\beta_{x,y}^2}}$ ($\sqrt{\overline{\beta_z^2}}$) in fine event pattern is equal to or larger (less) than that in non-fine event pattern. From pp to central Pb-Pb collisions, there is no obvious change in the non-fine event patterns. However, with increase of $\sqrt{s_{\rm NN}}$, the size in transverse plane decreases and that in longitudinal direction increases.

In Fig. 5, the scatter plots in p_x-p_y-p_z space are shown for the same collisions as in Fig. 4. The values of root-mean-squares $\sqrt{\overline{p_x^2}}$ for p_x, $\sqrt{\overline{p_y^2}}$ for p_y and $\sqrt{\overline{p_z^2}}$ for p_z, as well as the maximum $|p_x|$, $|p_y|$ and $|p_z|$ (i.e. $|p_x|_{\rm max}$, $|p_y|_{\rm max}$ and $|p_z|_{\rm max}$) for various systems and energies are listed in Table 6. One can see that both the event patterns in p_x-p_y-p_z space obtained from the rapidity-dependent and rapidity-independent spectra in pp collisions are rough cylindrical, though the size of fine event pattern is smaller than that of non-fine event patterns. From pp to central Pb-Pb collisions, there is no obvious change in the size of non-fine event patterns. With increase of $\sqrt{s_{\rm NN}}$, the size in transverse plane does not change obviously, and that in longitudinal direction increases obviously.

The scatter plots in Y_1-Y_2-Y space are shown in Fig. 6. The values of root-mean-squares $\sqrt{\overline{Y_1^2}}$ for Y_1, $\sqrt{\overline{Y_2^2}}$ for Y_2 and $\sqrt{\overline{Y^2}}$ for Y, as well as the maximum $|Y_1|$, $|Y_2|$ and $|Y|$ (i.e. $|Y_1|_{\rm max}$, $|Y_2|_{\rm max}$ and $|Y|_{\rm max}$) for various systems and energies are listed in Table 7. One can see that both the event patterns in Y_1-Y_2-Y space obtained from the rapidity-dependent and rapidity-independent spectra in pp collisions are rough rhombohedral, though the size of fine event pattern in transverse plane is larger than that of non-fine event patterns. However, from pp to central Pb-Pb collisions, there is no obvious change in the size of non-fine event patterns. With increase of $\sqrt{s_{\rm NN}}$, the size in transverse plane decreases, and that in longitudinal direction increases.

Now we move to a discussion of the properties of parameters obtained from Figs. 1–3 and listed in Tables 2–4. To show clearly the pictures for the dependences of parameters on Y, A and $\sqrt{s_{\rm NN}}$, Fig. 7 shows the correlations between (a) T_1 and Y, (b) T_2 and Y, (c) T and Y, as well as (d) k_1 and Y in pp collisions at different $\sqrt{s_{\rm NN}}$. Fig. 8 shows the correlations between (a) T_1 and $A^{1/3}$, (b) T_2 and $A^{1/3}$, (c) T and $A^{1/3}$, as well as (d) k_1 and $A^{1/3}$ at different $\sqrt{s_{\rm NN}}$. Fig. 9 shows the correlations between (a) δY and $A^{1/3}$, as well as (b) σ_Y and $A^{1/3}$ at different $\sqrt{s_{\rm NN}}$. One can see from Fig. 7 that, in pp collisions, T_1 does not change in central rapidity region and decreases in forward rapidity region, T_2 and T decrease, and k_1 increases with increase of Y. From Fig. 8 one can see that, from pp to central Pb-Pb collisions, T_1 decreases, T_2 increases and then saturates, T increases slightly, and k_1 decreases. From Fig. 9 one can see that δY and σ_Y do not change obviously. Meanwhile, from Figs. 7–9 one can see that, with increase of $\sqrt{s_{\rm NN}}$, T_1 does not change in central rapidity region and increases in forward rapidity region (or T_1 increases slightly), T_2

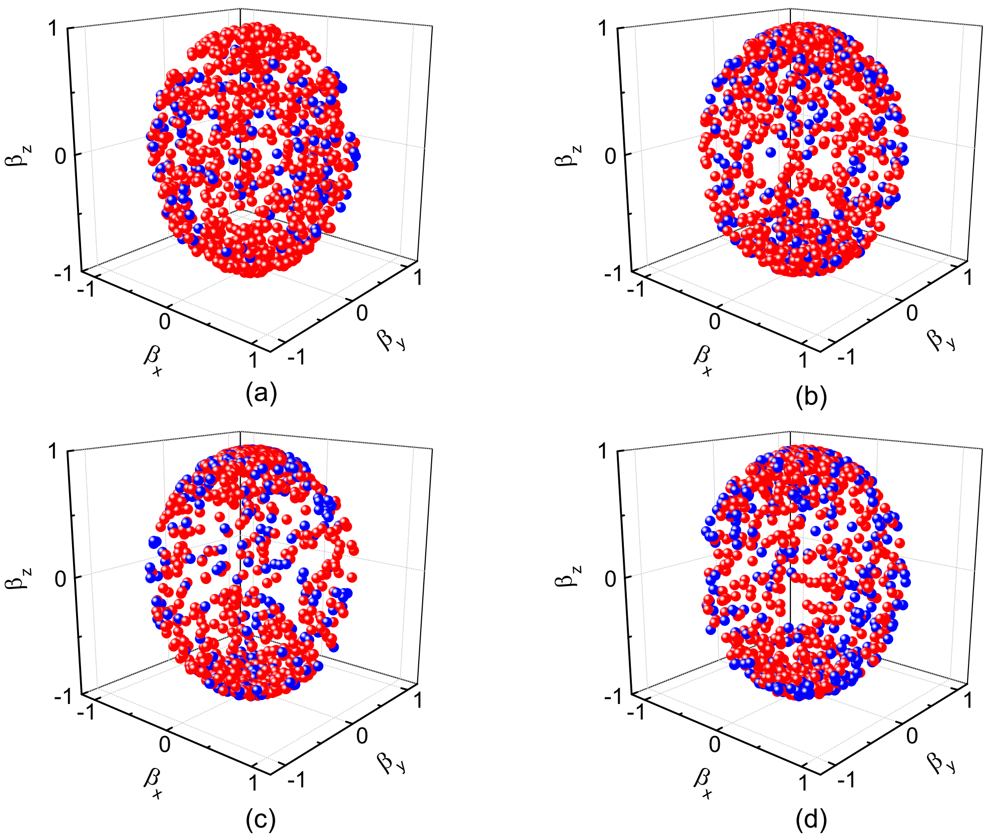

Fig. 4. (color online) The scatter plots of π^- at $\sqrt{s_{\rm NN}} = 6.3$ GeV in β_x-β_y-β_z space for (a) fine-event and (b) non-fine scatter plots in pp collisions, and for non-fine scatter plots for (c) Be-Be and (d) Pb-Pb collisions. The red and blue globules represent the contributions of the first and second components in the two-component standard distribution respectively. The number of π^- for each panel is 1000.

Table 5. Values of the root-mean-squares $\sqrt{\overline{\beta_x^2}}$ for β_x, $\sqrt{\overline{\beta_y^2}}$ for β_y and $\sqrt{\overline{\beta_z^2}}$ for β_z, and the maximum $|\beta_x|$, $|\beta_y|$ and $|\beta_z|$ ($|\beta_x|_{\rm max}$, $|\beta_y|_{\rm max}$ and $|\beta_z|_{\rm max}$) corresponding to the scatter plots for different collisions (see examples in Fig. 4). Both the root-mean-squares and the maximum velocity components are in the units of c.

Type	$\sqrt{s_{\rm NN}}$/GeV	$\sqrt{\overline{\beta_x^2}}$	$\sqrt{\overline{\beta_y^2}}$	$\sqrt{\overline{\beta_z^2}}$	$\lvert\beta_x\rvert_{\rm max}$	$\lvert\beta_y\rvert_{\rm max}$	$\lvert\beta_z\rvert_{\rm max}$
Fine pp	6.3	0.461 ± 0.009	0.454 ± 0.008	0.611 ± 0.008	0.984	0.965	0.989
	7.7	0.439 ± 0.009	0.433 ± 0.009	0.636 ± 0.008	0.990	0.966	0.991
	8.8	0.431 ± 0.009	0.426 ± 0.009	0.650 ± 0.008	0.964	0.975	0.995
	12.3	0.402 ± 0.010	0.395 ± 0.009	0.684 ± 0.008	0.974	0.979	0.994
	17.3	0.372 ± 0.010	0.371 ± 0.010	0.716 ± 0.007	0.982	0.967	0.997
Non-fine pp	6.3	0.425 ± 0.008	0.418 ± 0.008	0.727 ± 0.007	0.972	0.985	0.998
	7.7	0.418 ± 0.008	0.407 ± 0.008	0.743 ± 0.007	0.974	0.976	0.998
	8.8	0.409 ± 0.008	0.405 ± 0.008	0.754 ± 0.007	0.970	0.991	0.999
	12.3	0.391 ± 0.008	0.384 ± 0.008	0.781 ± 0.007	0.975	0.970	0.998
	17.3	0.371 ± 0.009	0.365 ± 0.008	0.804 ± 0.007	0.975	0.964	0.999
Central Be-Be	6.3	0.401 ± 0.008	0.390 ± 0.008	0.765 ± 0.007	0.943	0.954	0.997
	7.7	0.393 ± 0.008	0.381 ± 0.008	0.778 ± 0.007	0.961	0.966	0.998
	8.8	0.385 ± 0.008	0.378 ± 0.008	0.785 ± 0.007	0.973	0.976	0.998
	12.3	0.379 ± 0.009	0.366 ± 0.009	0.801 ± 0.007	0.963	0.978	0.999
	17.3	0.366 ± 0.009	0.353 ± 0.009	0.818 ± 0.006	0.968	0.975	0.999
Central Ar-Sc	6.3	0.421 ± 0.008	0.405 ± 0.008	0.744 ± 0.007	0.973	0.984	0.997
	7.7	0.412 ± 0.008	0.399 ± 0.008	0.756 ± 0.007	0.960	0.983	0.998
	8.8	0.403 ± 0.008	0.391 ± 0.008	0.768 ± 0.007	0.974	0.972	0.999
	12.3	0.385 ± 0.008	0.384 ± 0.008	0.787 ± 0.007	0.963	0.983	0.999
	17.3	0.368 ± 0.009	0.367 ± 0.009	0.807 ± 0.007	0.991	0.978	0.999
Central Pb-Pb	6.3	0.417 ± 0.008	0.409 ± 0.008	0.741 ± 0.007	0.969	0.984	0.998
	7.6	0.407 ± 0.008	0.400 ± 0.008	0.757 ± 0.007	0.954	0.981	0.998
	8.8	0.404 ± 0.008	0.395 ± 0.008	0.763 ± 0.007	0.951	0.995	0.999
	12.3	0.391 ± 0.008	0.384 ± 0.008	0.781 ± 0.007	0.975	0.970	0.998
	17.3	0.378 ± 0.009	0.364 ± 0.009	0.798 ± 0.007	0.961	0.981	0.999

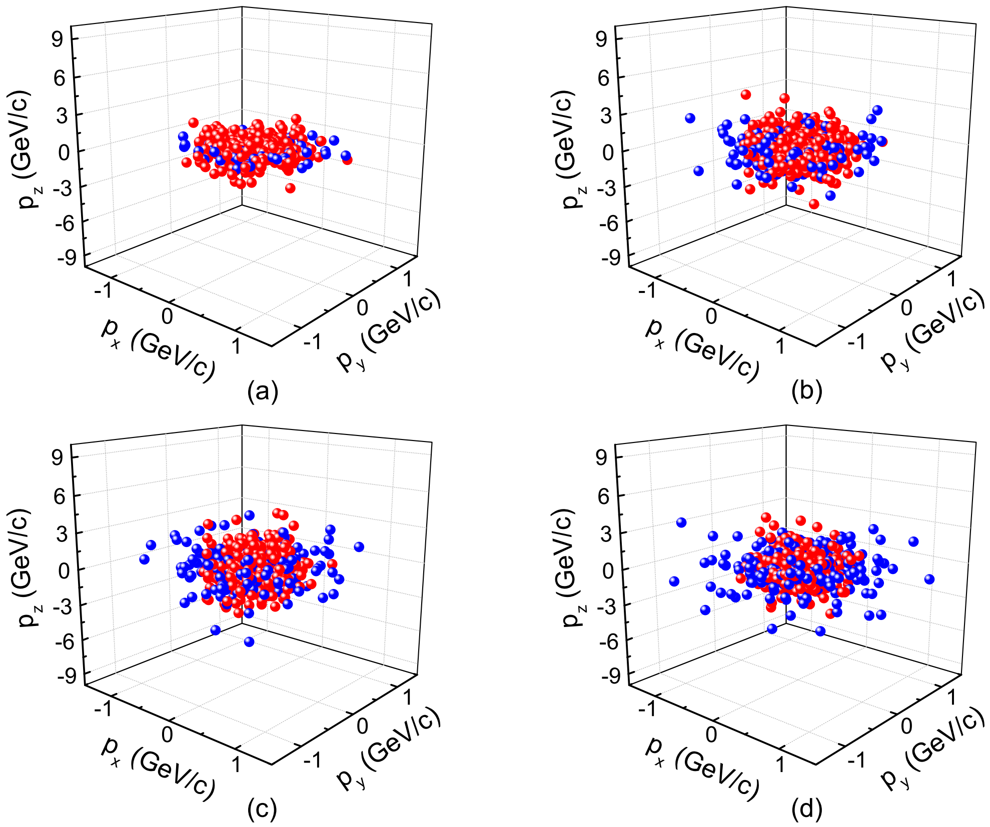

Fig. 5. (color online) Same as Fig. 4, but for p_x-p_y-p_z space.

Table 6. Values of the root-mean-squares $\sqrt{\overline{p_x^2}}$ for p_x, $\sqrt{\overline{p_y^2}}$ for p_y and $\sqrt{\overline{p_z^2}}$ for p_z, and the maximum $|p_x|$, $|p_y|$ and $|p_z|$ ($|p_x|_{\max}$, $|p_y|_{\max}$ and $|p_z|_{\max}$) corresponding to the scatter plots for different collisions (see examples in Fig. 5). All the root-mean-squares and the maximum momentum components are in the units of GeV/c.

Type	$\sqrt{s_{\rm NN}}$/GeV	$\sqrt{\overline{p_x^2}}$	$\sqrt{\overline{p_y^2}}$	$\sqrt{\overline{p_z^2}}$	$\lvert p_x\rvert_{\max}$	$\lvert p_y\rvert_{\max}$	$\lvert p_z\rvert_{\max}$
Fine pp	6.3	0.262 ± 0.008	0.242 ± 0.007	0.437 ± 0.017	1.195	0.923	2.359
	7.7	0.254 ± 0.008	0.233 ± 0.007	0.483 ± 0.019	1.275	0.925	2.573
	8.8	0.258 ± 0.008	0.240 ± 0.007	0.535 ± 0.021	1.235	0.934	2.653
	12.3	0.252 ± 0.009	0.231 ± 0.007	0.653 ± 0.028	1.315	0.964	3.543
	17.3	0.232 ± 0.008	0.226 ± 0.009	0.791 ± 0.038	1.055	1.364	4.470
Non-fine pp	6.3	0.288 ± 0.008	0.278 ± 0.008	0.878 ± 0.033	1.329	1.100	5.037
	7.7	0.298 ± 0.009	0.285 ± 0.008	0.982 ± 0.037	1.348	1.118	5.659
	8.8	0.302 ± 0.009	0.292 ± 0.009	1.095 ± 0.054	1.367	1.356	8.376
	12.3	0.303 ± 0.009	0.292 ± 0.009	1.276 ± 0.050	1.367	1.356	6.306
	17.3	0.304 ± 0.009	0.293 ± 0.009	1.531 ± 0.056	1.396	1.397	7.439
Central Be-Be	6.3	0.286 ± 0.009	0.276 ± 0.009	0.997 ± 0.032	1.358	1.346	4.115
	7.7	0.292 ± 0.009	0.283 ± 0.009	1.215 ± 0.045	1.367	1.356	6.338
	8.8	0.302 ± 0.009	0.294 ± 0.009	1.284 ± 0.050	1.405	1.407	6.414
	12.3	0.309 ± 0.010	0.299 ± 0.010	1.487 ± 0.056	1.425	1.437	7.794
	17.3	0.315 ± 0.010	0.305 ± 0.010	1.809 ± 0.072	1.444	1.447	9.762
Central Ar-Sc	6.3	0.308 ± 0.009	0.299 ± 0.010	0.911 ± 0.031	1.313	1.471	4.078
	7.7	0.312 ± 0.010	0.311 ± 0.010	1.012 ± 0.037	1.226	1.422	5.120
	8.8	0.313 ± 0.010	0.297 ± 0.009	1.113 ± 0.042	1.437	1.324	5.687
	12.3	0.299 ± 0.009	0.311 ± 0.010	1.312 ± 0.052	1.157	1.378	8.056
	17.3	0.311 ± 0.009	0.320 ± 0.010	1.683 ± 0.070	1.264	1.397	9.010
Central Pb-Pb	6.3	0.309 ± 0.009	0.312 ± 0.011	0.918 ± 0.033	1.421	1.559	4.422
	7.6	0.312 ± 0.010	0.319 ± 0.011	1.091 ± 0.042	1.226	1.422	5.299
	8.8	0.326 ± 0.010	0.331 ± 0.012	1.156 ± 0.054	1.546	1.569	9.169
	12.3	0.303 ± 0.009	0.292 ± 0.009	1.276 ± 0.050	1.367	1.356	6.306
	17.3	0.312 ± 0.009	0.314 ± 0.011	1.684 ± 0.067	1.290	1.522	8.891

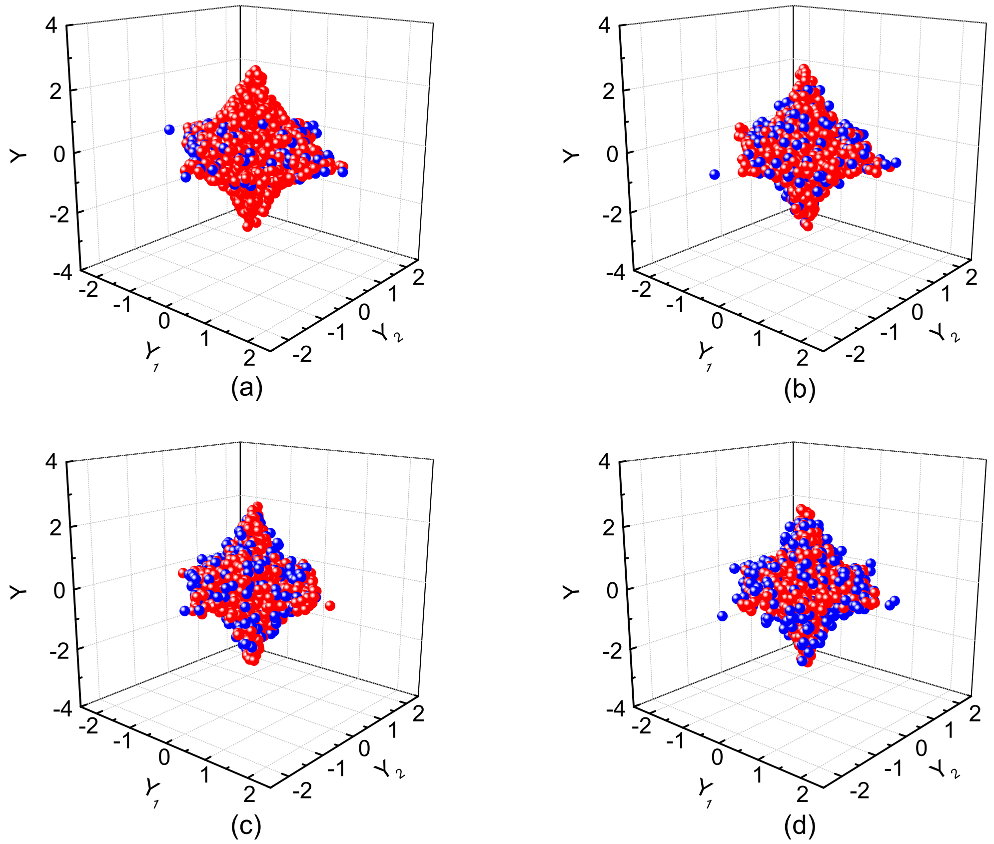

Fig. 6. (color online) Same as Fig. 4, but for Y_1-Y_2-Y space.

Table 7. Values of the root-mean-squares $\sqrt{\overline{Y_1^2}}$ for Y_1, $\sqrt{\overline{Y_2^2}}$ for Y_2 and $\sqrt{\overline{Y^2}}$ for Y, and the maximum $|Y_1|$, $|Y_2|$ and $|Y|$ ($|Y_1|_{\max}$, $|Y_2|_{\max}$ and $|Y|_{\max}$) corresponding to the scatter plots for different collisions (see examples in Fig. 6).

Type	$\sqrt{s_{\rm NN}}$/GeV	$\sqrt{\overline{Y_1^2}}$	$\sqrt{\overline{Y_2^2}}$	$\sqrt{\overline{Y^2}}$	$\|Y_1\|_{\max}$	$\|Y_2\|_{\max}$	$\|Y\|_{\max}$
Fine pp	6.3	0.626 ± 0.017	0.605 ± 0.016	0.938 ± 0.020	2.404	2.014	2.593
	7.7	0.602 ± 0.018	0.580 ± 0.016	1.001 ± 0.020	2.657	2.022	2.688
	8.8	0.579 ± 0.016	0.570 ± 0.016	1.049 ± 0.021	2.000	2.180	2.969
	12.3	0.553 ± 0.018	0.533 ± 0.017	1.158 ± 0.022	2.168	2.285	2.922
	17.3	0.507 ± 0.008	0.500 ± 0.017	1.285 ± 0.024	2.364	2.049	3.179
Non-fine pp	6.3	0.547 ± 0.015	0.533 ± 0.015	0.938 ± 0.020	2.120	2.448	2.593
	7.7	0.537 ± 0.015	0.521 ± 0.015	1.001 ± 0.020	2.169	2.208	2.688
	8.8	0.528 ± 0.016	0.520 ± 0.016	1.049 ± 0.021	2.098	2.708	2.969
	12.3	0.504 ± 0.016	0.487 ± 0.015	1.158 ± 0.022	2.183	2.091	2.922
	17.3	0.478 ± 0.016	0.460 ± 0.015	1.285 ± 0.024	2.185	2.003	3.179
Central Be-Be	6.3	0.510 ± 0.014	0.493 ± 0.015	1.052 ± 0.020	1.761	1.879	2.558
	7.7	0.509 ± 0.016	0.487 ± 0.015	1.147 ± 0.022	1.953	2.022	2.766
	8.8	0.494 ± 0.016	0.479 ± 0.015	1.169 ± 0.022	2.137	2.206	2.935
	12.3	0.493 ± 0.016	0.472 ± 0.016	1.263 ± 0.023	1.990	2.250	2.970
	17.3	0.477 ± 0.017	0.457 ± 0.017	1.376 ± 0.025	2.053	2.185	3.194
Central Ar-Sc	6.3	0.542 ± 0.015	0.516 ± 0.015	0.977 ± 0.019	2.147	2.408	2.552
	7.7	0.527 ± 0.015	0.512 ± 0.016	1.026 ± 0.020	1.945	2.382	2.647
	8.8	0.516 ± 0.015	0.500 ± 0.015	1.090 ± 0.021	2.173	2.122	2.993
	12.3	0.494 ± 0.015	0.499 ± 0.017	1.190 ± 0.022	1.985	2.366	2.991
	17.3	0.474 ± 0.017	0.474 ± 0.016	1.315 ± 0.024	2.708	2.259	3.140
Central Pb-Pb	6.3	0.536 ± 0.015	0.529 ± 0.016	0.975 ± 0.019	2.072	2.420	2.587
	7.6	0.517 ± 0.014	0.519 ± 0.016	1.056 ± 0.021	1.879	2.320	2.792
	8.8	0.516 ± 0.015	0.525 ± 0.019	1.077 ± 0.021	1.840	2.960	2.993
	12.3	0.504 ± 0.016	0.487 ± 0.015	1.158 ± 0.022	2.183	2.091	2.922
	17.3	0.486 ± 0.016	0.465 ± 0.016	1.312 ± 0.025	1.952	2.315	3.185

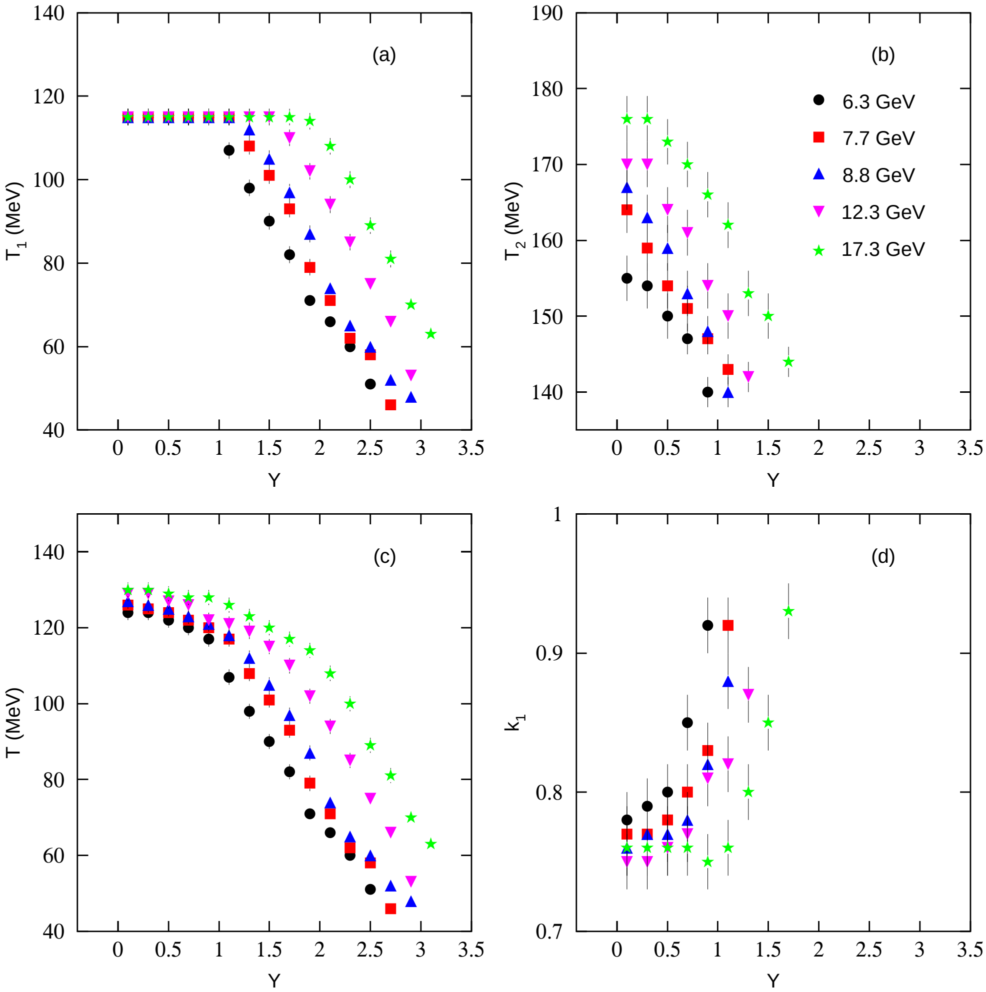

Figs. 7. (color online) Correlations between (a) T_1 and Y, (b) T_2 and Y, (c) T and Y, as well as (d) k_1 and Y in pp collisions at different $\sqrt{s_{\rm NN}}$. The results corresponding to different $\sqrt{s_{\rm NN}}$ are represented by different symbols marked in the panels.

and T increase, k_1 decreases, and δY and σ_Y increase.

The observed dependencies of the parameters can be treated as follows in the sense of possible scenarios of the particle production process.

The observations in Fig. 7, namely the increase of the temperature parameters T_1, T_2, and then the increase of the effective temperature T being their combination, with decrease of the rapidity Y can be explained by an increase of the excitation energy due to the increasing energy deposition by the system as one moves from the large absolute rapidities (above unity, the forward rapidity region) to the lower ones (central region). In the forward rapidity region it is natural to assume the particles having a shorter mean-free path as less energy is deposited, while in the central rapidity region, the particles can be considered to scatter with larger mean-free path as getting larger excitation energy. This picture can be associated with the liquid-like state in the former case against the gas-like state in the latter one. Within this consideration, the first component characterized by T_1 temperature can be assigned to the liquid-like state, and the second component with T_2 temperature to the gas-like state. Then, the temperature of a phase transition from the liquid-like state to the gas-like one gets 115 MeV (see Fig. 7(a)) with no flow effect being excluded. This also makes it understandable the T_1 parameter to be of a constant value as one reaching a critical temperature value. One however should note that in the central rapidity region, the mixture of the gas-like and liquid-like states is expected, as it is seen from the T-parameter behavior.

The system-size dependences shown in Fig. 8 find their following explanations. For the liquid-like state, one expects lower temperature in larger systems due to the energy loss, as it is observed in Fig. 8(a). On the contrary, for the gas-like component, more energy depo-

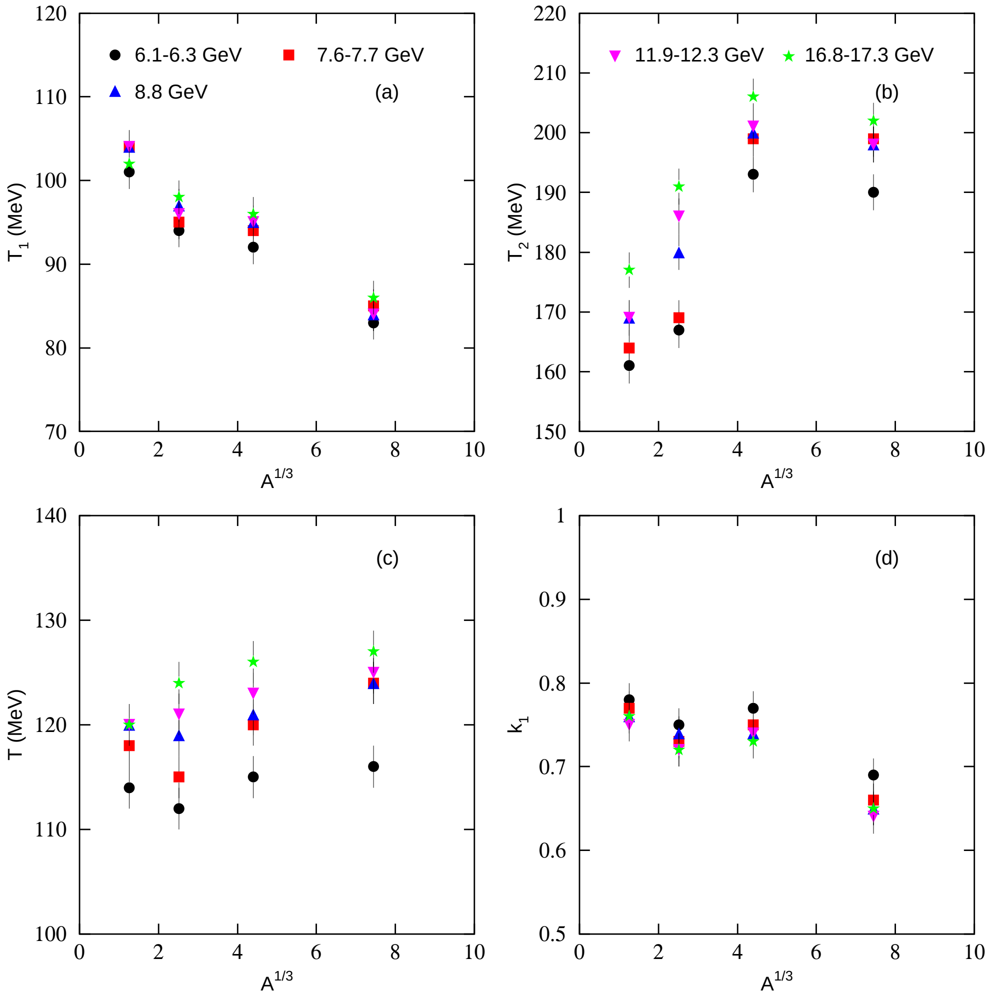

Figs. 8. (color online) Correlations between (a) T_1 and $A^{1/3}$, (b) T_2 and $A^{1/3}$, (c) T and $A^{1/3}$, as well as (d) k_1 and $A^{1/3}$ at different $\sqrt{s_{\mathrm{NN}}}$.

sition should be expected in large system due to nuclear stopping and hence higher temperature as it is seen in Fig. 8(b).

The behavior of the effective temperature parameter T is a combination of the contributions of T_1, T_2 and the rate k_1. From Figs. 7 and 8, one can see that T increases and k_1 decreases as one moves from the forward region to the central one and as the collision energy and the system size increase. These dependences can be explained by the general increase of the energy deposition. Let us remind that the T is the effective temperature which means it does not exclude the particle-flow effect. As soon as one excludes the flow effect, the lower temperature value can be obtained characterizing the interacting system a freeze-out, the so-called freeze-out temperature.

The dependences observed in Fig. 9 can be treated as the following features of the particle production process. Assuming the binary nucleon-nucleon collisions being the main internal process not only in small system as pp but also in such a large system as Pb-Pb is, the rapidity shift independence of the system size is expected as it is generally confirmed by the observation in Fig. 9. In the meantime, the increase of the rapidity shift with the collision energy would be naturally explained by the increase of the penetrating power.

It should be noted that the functions used in the above discussions are only one choice to fit the experimental p_T or m_T and Y spectra. One can also choose other functions to fit the same experimental spectra and to obtain properties of other parameters. One can consider the Tsallis distribution to fit the transverse spectra as widely used, see e.g. ref. [8]. However, the effective temperature considered in the present work and one used in the Tsallis approach cannot be compared directly as being different parameters.

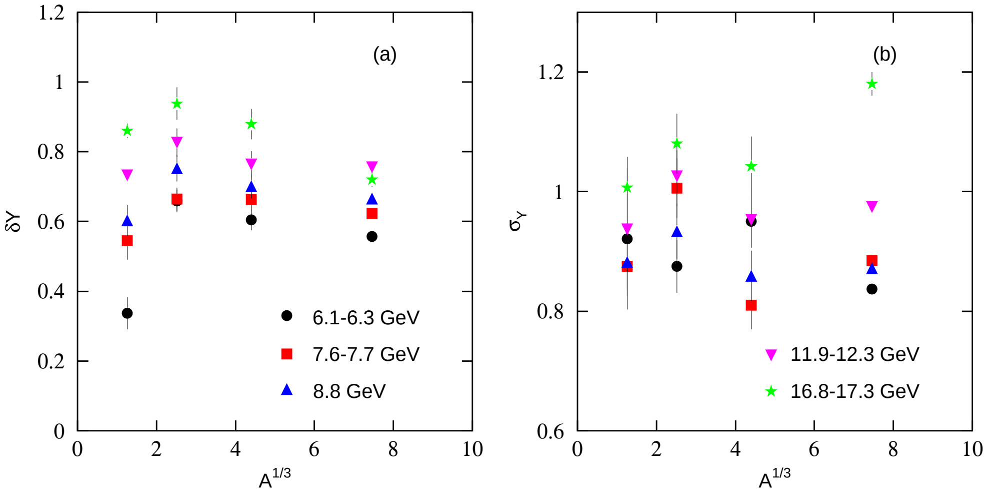

Figs. 9. (color online) Correlations between (a) δY and $A^{1/3}$, as well as (b) σ_Y and $A^{1/3}$ at different $\sqrt{s_{\rm NN}}$.

4 Conclusions

We summarize here our main observations and conclusions.

(a) We have used the hybrid model to fit the $p_{\rm T}$ or $m_{\rm T}$ and Y spectra of π^- produced in pp and central Be-Be, Ar-Sc, as well as Pb-Pb collisions at the SPS at its BES energies which cover an energy range from 6.1 to 17.3 GeV. For the $p_{\rm T}$ or $m_{\rm T}$ spectra, the (two-component) standard distribution is used. For the Y spectra, the double-Gaussian distribution is used. The model results are in good agreement with the experimental data of the NA61/SHINE and NA49 Collaborations. All parameter values and event patterns extracted from the fits reflect the properties of interaction system at the stage of kinetic freeze-out.

(b) The extracted parameters show abundant features. In pp collisions, the distribution first component effective temperature T_1 does not change in central rapidity region and decreases in forward rapidity region, the distribution second component effective temperature T_2 and the combined effective temperature T decrease, and the fraction parameter k_1 increases with increase of Y. From pp to central Pb-Pb collisions, T_1 decreases, T_2 increases and then saturates, T increases slightly, k_1 decreases, and δY and σ_Y do not change obviously. Meanwhile, with increase of $\sqrt{s_{\rm NN}}$, T_1 does not change in central rapidity region and increases in forward rapidity region (or T_1 increases slightly), T_2 and T increase, k_1 decreases, and δY and σ_Y increase.

(c) The two types of event patterns are extracted in pp collisions. The fine patterns are extracted from the $p_{\rm T}$ spectra which depend on rapidity, and the other, non-fine patterns are from the rapidity-independent $m_{\rm T}$ spectra which is only measured at mid-rapidity. Both the event patterns in β_x-β_y-β_z space are spherical, though $\sqrt{\beta^2_{x,y}}$ ($\sqrt{\beta^2_z}$) in fine event pattern is equal to or larger (less) than that in non-fine event pattern. Both the event patterns in p_x-p_y-p_z space are rough cylindrical, though the size of fine event pattern is less than that of non-fine event patterns. Both the event patterns in Y_1-Y_2-Y space are rough rhombohedral, though the size of fine event pattern in transverse plane is larger than that of non-fine event patterns.

(d) From pp to central Pb-Pb collisions, there is no obvious change in the shape and size of non-fine event patterns. With increase of $\sqrt{s_{\rm NN}}$, in both the three-dimensional velocity and rapidity spaces, the size of event pattern in transverse plane decreases and that in longitudinal direction increases. Meanwhile, in the three-dimensional momentum space, the size of event pattern in transverse plane does not change obviously, and that in longitudinal direction increases obviously. These observations are useful in the understanding of particle production in different types of collisions such as the collisions at the BES at the Relativistic Heavy Ion Collider.

Acknowledgments

This work was supported by the National Natural Science Foundation of China under Grant Nos. 11575103 and 11747319, the Shanxi Provincial Natural Science Foundation under Grant No. 201701D121005, and the Fund for Shanxi “1331 Project” Key Subjects Construction.

References

[1] R. Aaij et al. (LHCb collaboration), JHEP **10**: 172 (2015)

[2] J. Adam et al. (ALICE Collaboration), Phys. Lett. B **753**: 319 (2016)

[3] G. Aad et al. (ATLAS Collaboration), Phys. Lett. B **757**: 334 (2016)

[4] V. Khachatryan et al. (CMS Collaboration), Phys. Lett. B **758**: 152 (2016)

[5] J. L. Synge, *The Relativistic Gas* (North-Holland, Amsterdam, The Netherlands, 1957)

[6] P. Z. Ning, L. Li, and D. F. Min, *Foundation of Nuclear Physics: Nucleons and Nuclei* (Higher Education Press, Beijing, China, 2003)

[7] C. D. Dermer, Astrophys. J. **280**: 328 (1984)

[8] J. Cleymans and D. Worku, Eur. Phys. J. A **48**: 160 (2012)

[9] C. Tsallis, J. Stat. Phys. **52**: 479 (1988)

[10] G. Wilk and Z. Włodarczyk, Eur. Phys. J. A **40**: 299 (2009)

[11] T. S. Biró, Eur. Phys. J. A **40**: 255 (2009)

[12] T. S. Biró, G. Purcsel, and K. Ürmössy, Eur. Phys. J. A **40**: 325 (2009)

[13] W. M. Alberico and A. Lavagno, Eur. Phys. J. A **40**: 313 (2009)

[14] H. Zheng and L. L. Zhu, Adv. High Energy Phys. **2016**: 9632126 (2016)

[15] F.-H. Liu, Y.-Q. Gao, T. Tian, and B.-C. Li, Eur. Phys. J. A **50**: 94 (2014)

[16] G. Arnison et al. (UA1 Collaboration), Phys. Lett. B **118**: 167 (1982)

[17] R. Odorico, Phys. Lett. B **118**: 151 (1982)

[18] M. Biyajima, T. Mizoguchi, and N. Suzuki, Int. J. Mod. Phys. A **32**: 1750057 (2017)

[19] J. Schwinger, Phys. Rev. **82**: 664 (1951)

[20] R.-C. Wang and C.-Y. Wong, Phys. Rev. D **38**: 348 (1988)

[21] C.-Y. Wong, *Introduction to High Energy Heavy Ion Collisions* (World Scientific, Singapore, 1994)

[22] P. Braun-Munzinger, K. Redlich, and J. Stachel, in *Quark-Gluon Plasma 3*, edited by R. C. Hwa and X.-N. Wang (World Scientific, Singapore, 2004) arXiv:nucl-th/0304013 (2004)

[23] E. Schnedermann, J. Sollfrank, and U. Heinz, Phys. Rev. C **48**: 2462 (1993)

[24] B. I. Abelev et al. (STAR Collaboration), Phys. Rev. C **79**: 034909 (2009)

[25] B. I. Abelev et al. (STAR Collaboration), Phys. Rev. C **81**: 024911 (2010)

[26] Z. B. Tang, Y. C. Xu, L. J. Ruan, G. van Buren, F. Q. Wang, and Z. B. Xu, Phys. Rev. C **79**: 051901(R) (2009)

[27] L. D. Landau, Izvestiya Akademii Nauk SSSR: Seriya Fizicheskaya **17**, 51 (1953), English translation in *Collected Papers of L. D. Landau* (Pergamon, Oxford), p. 569 (1965)

[28] S. Z. Belenkij and L. D. Landau, Soviet Physics Uspekhi **56**, 309 (1955), the shorten English translation in Nuovo Cim. Suppl. **3S10**: 15 (1956)

[29] P. Carruthers and M. Doung-van, Phys. Rev. D **8**: 859 (1973)

[30] I. G. Bearden et al. (BRAHMS Collaboration), Phys. Rev. Lett. **88**: 202301 (2002)

[31] M. Murray for the BRAHMS Collaboration, J. Phys. G. **30**: S667 (2004)

[32] I. G. Bearden et al. (BRAHMS Collaboration), Phys. Rev. Lett. **94**: 162301 (2005)

[33] M. Murray for the BRAHMS Collaboration, J. Phys. G **35**: 044015 (2008)

[34] C.-Y. Wong, Phys. Rev. C **78**: 054902 (2008)

[35] E. K. G. Sarkisyan and A. S. Sakharov, AIP Conf. Proc. **828**: 35 (2006)

[36] E. K. G. Sarkisyan and A. S. Sakharov, Eur. Phys. J. C **70**: 533 (2010)

[37] E. K. G. Sarkisyan, A. N. Mishra, R. Sahoo, and A. S. Sakharov, Phys. Rev. D **93**: 054046 (2016)

[38] Z. J. Jiang, H. P. Deng, Y. Zhang, and H. L. Zhang, Nucl. Phys. Rev. (China) **32**: 398 (2015)

[39] Z. J. Jiang and H. L. Zhang, Mod. Phys. Lett. A **29**: 1450130 (2014)

[40] Z. J. Jiang, Y. Zhang, H. L. Zhang, and H. P. Deng, Nucl. Phys. A **941**: 188 (2015)

[41] Y.-H. Chen, G.-X. Zhang, and F.-H. Liu, Adv. High Energy Phys. **2015**: 614090 (2015)

[42] Y.-H. Chen, F.-H. Liu, S. Fakhraddin, M. A. Rahim, and M.-Y. Duan, J. Phys. G **44**: 025103 (2017)

[43] Y.-H. Chen, F.-H. Liu, and R. A. Lacey, Adv. High Energy Phys. **2016**: 9876253 (2016)

[44] Y.-H. Chen and F.-H. Liu, Eur. Phys. J. A **53**: 230 (2017)

[45] N. Abgrall et al. (NA61/SHINE Collaboration), Eur. Phys. J. C **74**: 2794 (2014)

[46] S. Pulawski on behalf of the NA61/SHINE Collaboration, EPJ Web Conf. **164**: 07033 (2017)

[47] C. Alt et al. (NA49 Collaboration), Phys. Rev. C **77**: 024903 (2008)

[48] S. V. Afanasiev et al. (NA49 Collaboration), Phys. Rev. C **66**: 054902 (2002)

[49] S. Pulawski for the NA61/SHINE Collaboration, Acta Phys. Pol. B **46**: 2381 (2015)

[50] A. Aduszkiewicz for the NA61/SHINE Collaboration, Nucl. Phys. A **967**: 35 (2017)

[51] S. S. Adler et al. (PHENIX Collaboration), Phys. Rev. C **69**: 034909 (2004)

[52] P. Braun-Munzinger, D. Magestro, K. Redlich, and J. Stachel, Phys. Lett. B **518**: 41 (2001)

[53] S. Takeuchi, K. Murase, T. Hirano, P. Huovinen, and Y. Nara, Phys. Rev. C **92**: 044907 (2015)

[54] C. Gale, Y. Hidaka, S. Jeon, S. Lin, J.-F. Paquet, R. D. Pisarski, D. Satow, V. V. Skokov, and G. Vujanovic, Phys. Rev. Lett. **114**: 072301 (2015)

[55] A. Andronic, P. Braun-Munzinger, and J. Stachel, Nucl. Phys. A **772**: 167 (2006)

[56] J. Cleymans, H. Oeschler, K. Redlich, and S. Wheaton, Phys. Rev. C **73**: 034905 (2006)

[57] A. Andronic, P. Braun-Munzinger, and J. Stachel, Acta Phys. Pol. B **40**: 1005 (2009)

[58] A. Andronic, P. Braun-Munzinger, and J. Stachel, Nucl. Phys. A **834**: 237c (2010)

[59] C. Forbes, M. Evans, N. Hastings, and B. Peacock, *Statistical Distributions* (Fourth Edition, John Wiley & Sons, Inc., Hoboken, New Jersey, USA, p. 147, 2011)

[60] A. Aduszkiewicz et al. (NA61/SHINE Collaboration), Eur. Phys. J. C **77**: 671 (2017)

[61] S. Das for the STAR collaboration, EPJ Web of Conf. **90**: 08007 (2015)